

Reynolds Number and Flow Regime Analysis Using MATLAB and CFD Simulation

Abdelrahman Emad, Zyad Hamed, Yomna Sabry, Sulaiman Alfozan, Hamdy Ahmed
Team 4

Abstract—Understanding how fluids behave within biological and biomedical systems is crucial for designing safe and efficient medical devices and models. In this task, we explored the fundamental concepts of biofluid mechanics through both computational and analytical approaches. Using a MATLAB-based application, we calculated the Reynolds number for various fluids and geometries, classified flow regimes, visualized velocity profiles, and analyzed how the friction factor changes with Reynolds number and surface roughness. The app we developed served as both a calculator and an educational simulation tool, allowing us to interactively study laminar, transitional, and turbulent behaviors under realistic conditions with predefined examples.

To further this analysis, numerical flow simulations were conducted on various two-dimensional and three-dimensional geometries utilizing a multiphysics solver. These models demonstrated how flow develops and transforms across complex biomedical-like conduits, including elbows, bifurcations, and multi-inlet tubes. The resulting velocity fields, contours, and streamlines from these simulations clearly illustrated phenomena such as flow acceleration at bends, regions of elevated wall shear, and the transition from laminar to turbulent flow.

Overall, integrating the analytical MATLAB tools with CFD simulations provided us with a more understanding of fluid flow phenomena in internal conduits. This report links theoretical correlations with visual, physical interpretation—bridging fundamental fluid mechanics with its biomedical applications, such as blood flow modeling, catheter design, and fluid transport in artificial organs.

I. INTRODUCTION

Fluid flow plays a vital role in both engineering and biomedical systems, from blood circulation and cerebrospinal fluid motion to airflow and device perfusion. In biomedical engineering, understanding how fluids move through vessels, catheters, and airways is essential for safe and efficient device design. Flow behaviour governs pressure, shear stress, and mass transport, while instability or turbulence can increase energy losses or cause physiological complications. Studying these flow regimes is therefore fundamental to improving biomedical devices and ensuring patient safety.

The Reynolds number (Re) is a dimensionless quantity that characterises the type of fluid flow by comparing inertial forces to viscous forces. It is expressed as $Re = \frac{\rho V D}{\mu}$, where ρ is the fluid density, V is the average velocity, D is the characteristic length or hydraulic diameter, and μ is the dynamic viscosity. Low Reynolds numbers indicate viscous-dominated, orderly motion known as laminar flow, while high values signify inertia-dominated, chaotic turbulent flow. The transition between these regimes typically occurs within the range $2000 \leq Re < 4000$. In addition to flow classification,

the friction factor (f) is used to quantify the resistance to motion within a conduit. It relates the wall shear stress and pressure loss to the flow regime and surface roughness, where $f = 64/Re$ describes laminar flow and empirical correlations such as the Swamee Jain equation are applied for turbulent conditions.

For this assignment, we aimed to investigate and analyse the relationship among the Reynolds number, flow regime, and friction factor using both analytical modelling and computational simulation. A MATLAB application was developed to calculate the Reynolds number for different fluids and geometries, classify the flow regime, and plot the corresponding velocity profiles and friction factor trends. In addition to the analytical work, computational fluid dynamics (CFD) simulations were performed on different geometries to visualise how the flow evolves and transitions from laminar to turbulent conditions. Integrating these two methods allowed us to connect theoretical predictions with physical visualisation, leading to a deeper understanding of internal flow behaviour in biomedical applications.

This report is divided into five main parts, along with one bonus section:

- **Part 1** focuses on calculating the Reynolds number and classifying flow regimes for various fluids and geometries.
- **Part 2** presents the visualisation of velocity profiles for laminar and turbulent conditions.
- **Part 3** analyses the relationship between the Reynolds number and the Darcy friction factor.
- **Part 4** introduces the interactive MATLAB calculator developed for user input and flow regime identification.
- **Part 5** illustrates conceptual visualisations of laminar, transitional, and turbulent flows.

Finally, the **bonus section** includes computational fluid dynamics (CFD) simulations that demonstrate the development and transition of flow within different geometrical models.

II. METHODOLOGY

A. Backend Design and Computational Framework

The backend system functions as the computational core responsible for executing all analytical calculations, data processing, and result generation. It was developed in a modular structure composed of several interrelated functions, each assigned to a distinct analytical or graphical task to ensure clarity, maintainability, and future scalability.

The computational process follows a dispatcher-based logic in which specific operations are triggered according to the required analysis type. Dedicated modules were implemented to handle case analysis, velocity-profile plotting, friction-factor evaluation, and conceptual flow visualisation. This modular design allows each component to be updated independently without affecting the overall performance or accuracy of the tool.

Equations Implemented: The analytical calculations are based on fundamental principles of fluid mechanics and verified using standard references such as Cengel [1] and other reliable online resources. The Reynolds number (Re) was determined using

$$Re = \frac{\rho V D_h}{\mu}, \quad (1)$$

where ρ is the fluid density (kg/m^3), V is the mean velocity (m/s), D_h is the hydraulic diameter (m), and μ is the dynamic viscosity ($\text{Pa}\cdot\text{s}$). For non-circular conduits, the hydraulic diameter was evaluated as

$$D_h = \frac{4A}{P}, \quad (2)$$

where A represents the cross-sectional area and P the wetted perimeter. These relations were adapted for circular, rectangular, square, and annular geometries following established textbook formulations.

Flow Regime Classification: The calculated Reynolds number was used to categorise the flow regime according to conventional limits:

- **Laminar:** $Re < 2000$
- **Transitional:** $2000 \leq Re < 4000$
- **Turbulent:** $Re \geq 4000$

This classification guided both the selection of governing equations and the interpretation of results in subsequent analyses.

Friction Factor Models: The Darcy friction factor (f) quantifies flow resistance and is directly related to the pressure loss within the conduit. For laminar flow, it is defined as

$$f = \frac{64}{Re}. \quad (3)$$

For turbulent conditions, the Swamee–Jain explicit approximation [3] was employed:

$$f = \frac{0.25}{[\log_{10}\left(\frac{\varepsilon}{3.7} + \frac{5.74}{Re^{0.9}}\right)]^2}, \quad (4)$$

where ε denotes the absolute roughness of the pipe surface. This correlation offers an accurate, non-iterative solution to the Colebrook equation and was selected for its computational efficiency and reliability in turbulent-flow calculations.

Model predictions were validated by comparing the resulting f - Re relationship with the standard Moody chart, referencing data available from Nuclear Power Engineering Resources [4]. The results reproduced the expected laminar trend ($f \propto Re^{-1}$) and turbulent decay ($f \propto Re^{-0.25}$), showing consistent separation between smooth and rough surfaces.

Velocity Profile Formulation: For visualisation purposes, velocity profiles were computed analytically for both laminar and turbulent conditions:

$$u_{\text{laminar}}(r) = 2U \left(1 - \frac{r^2}{R^2}\right), \quad (5)$$

$$u_{\text{turbulent}}(r) = U_{\max} \left(1 - \frac{r}{R}\right)^{1/7}, \quad U_{\max} \approx \frac{U}{0.817}. \quad (6)$$

These expressions illustrate the parabolic nature of laminar flow and the flatter velocity distribution in turbulent flow. The profiles were compared with the reference diagrams provided in Cengel's Fluid Mechanics textbook and showed strong agreement with theoretical expectations.

Code Modularity and Structure: Each computational segment was designed to be reusable, transparent, and easily extendable. Parameters or equations can be modified without influencing other components of the framework. This modularity simplifies debugging and enables the integration of additional models, such as non-Newtonian biofluids or complex geometrical configurations. The overall design therefore achieves a balance between analytical accuracy, computational efficiency, and educational clarity.

B. Frontend Design and User Interface

The frontend was developed to provide a clear, intuitive, and interactive environment that connects users directly to the analytical and visual capabilities of the system. Its primary role is to collect input parameters, communicate with the computational backend, and display results in a structured and comprehensible manner. The design emphasises simplicity, educational value, and ease of use, allowing users to explore fluid behaviour without prior programming experience.

The interface was organised into five main tabs, each corresponding directly to one of the analytical parts described in the assignment requirements. This tab-based design ensured logical navigation, allowing users to progress sequentially from calculation to interpretation.

Calculator Tab (Part 4): The first tab functions as an interactive calculator for determining the Reynolds number, friction factor, and flow regime. Users input the necessary parameters, including fluid density, velocity, viscosity, and the relevant geometric dimensions. Upon calculation, the interface instantly displays the Reynolds number and the corresponding regime classification, with colour-coded indicators to distinguish laminar, transitional, and turbulent flow. Error handling was incorporated to identify missing or invalid entries, ensuring numerical stability and user guidance.

Predefined Cases Tab (Part 1): The second tab provides a comprehensive set of predefined flow scenarios covering various fluids, temperatures, and conduit geometries. These include water, air, blood, and cerebrospinal fluid at different temperatures and pipe dimensions. Each case automatically calculates the Reynolds number and friction factor, presenting the results in a sortable table for comparison and analysis. Selecting any case from the table triggers a direct update of the corresponding velocity profile and visual outputs, linking seamlessly with the backend computation.

Velocity Profiles Tab (Part 2): The third tab visualises velocity profiles for both laminar and turbulent flows. The system plots the parabolic distribution expected for laminar flow alongside the flatter 1/7-power-law distribution of turbulent flow, allowing direct comparison. These plots dynamically update based on the user-selected case or input conditions, reinforcing the physical understanding of how flow regimes influence velocity gradients across a cross-section.

Friction Factor Tab (Part 3): The fourth tab presents a logarithmic plot of the Darcy friction factor as a function of Reynolds number. The plot incorporates both the laminar and turbulent correlations, using the Swamee–Jain model for turbulent flow and the analytical $f = 64/Re$ relation for laminar flow. Transition boundaries are clearly indicated, and roughness variations are included to show how material properties affect flow resistance. This visual representation reinforces the relationship between flow regime and hydraulic losses.

Conceptual Flow Tab (Part 5): The final tab provides conceptual flow visualisations that compare laminar, transitional, and turbulent regimes through quiver plots. Each plot represents the direction and magnitude of velocity vectors, showing the evolution from smooth, parallel streamlines in laminar flow to disordered, chaotic motion in turbulence. These simplified representations complement the analytical results and strengthen conceptual understanding of regime differences.

Design Philosophy: The frontend design prioritised clarity and interactivity to support both analytical investigation and educational engagement. Tabs were labelled to follow the same logical structure as the analysis workflow, allowing users to progress naturally from fundamental calculations to advanced visualisation. Error handling, colour feedback, and real-time plotting features make the interface robust and accessible for biomedical engineering students studying biofluid mechanics. The combination of structured layout and interactive feedback transforms theoretical fluid-mechanics principles into a practical, user-driven experience.

C. Integration Between Backend and Frontend

The analytical backend and graphical frontend were developed as independent yet fully integrated components, linked through a structured dispatcher architecture. This design ensures a clear separation between the computational logic and the graphical user interface (GUI), allowing updates and debugging to occur efficiently without interdependence between code layers.

The interaction between both components follows a systematic workflow. When a user provides input parameters such as fluid density, velocity, or viscosity through the interface, the frontend transmits these values to the backend.

The backend then executes the corresponding computational routine—such as Reynolds number calculation, flow regime classification, or friction factor estimation—and returns the processed results to the interface. The frontend subsequently

updates all relevant plots and tables in real time, enabling immediate visualisation of analytical outcomes.

This separation of logic from presentation not only enhances maintainability but also ensures high modularity. Any modification to equations, parameters, or additional models can be implemented directly within the backend without altering the user interface. The structure simplifies debugging, facilitates code expansion, and allows future extensions such as the integration of non-Newtonian biofluid models or additional geometric configurations. The overall architecture therefore achieves both computational reliability and long-term adaptability.

D. Validation and Reference Alignment

To ensure accuracy and physical consistency, all analytical models and visual outputs were validated against well-established references and textbook data. The theoretical velocity profiles, friction factor relations, and flow regime classifications were cross-checked with figures and equations from Cengel's *Fluid Mechanics: Fundamentals and Applications* [1]. The parabolic velocity distribution for laminar flow and the flattened profile under turbulent conditions showed strong agreement with the referenced diagrams, confirming the correctness of the implemented relations.

The turbulent-flow friction factor correlation was verified using the Swamee–Jain explicit approximation as described by EngineerExcel [3]. The computationally derived f – Re curves reproduced the expected smooth decline across the turbulent region without requiring iterative solutions, validating both the numerical stability and the mathematical implementation of the model.

Additionally, the global behaviour of the Darcy friction factor was compared to the reference Moody chart available through Nuclear Power Engineering Resources [4]. The simulation produced the correct asymptotic trends: $f \propto Re^{-1}$ for laminar flow and a slower, logarithmic decay for turbulent flow. Variations in pipe roughness also resulted in the anticipated upward shifts in the friction factor, demonstrating sensitivity consistent with physical expectations.

At increasing Reynolds numbers, velocity profiles became progressively flatter, reflecting the transition from viscous-dominated to inertia-dominated flow behaviour. The conceptual quiver plots generated for laminar, transitional, and turbulent regimes exhibited the textbook characteristics of smooth streamlines, wavy instabilities, and fully developed chaotic motion, respectively. These outcomes confirmed that the analytical formulations, computational implementation, and visual representations were fully aligned with established fluid mechanics theory and experimental trends.

E. CFD Simulation Setup and Numerical Procedure

To extend the analytical MATLAB results into spatially resolved visualizations, a set of computational fluid dynamics (CFD) simulations was performed using **FEATool Multiphysics**, a MATLAB-integrated multiphysics environment. The purpose of this extension was to reproduce the same

physical concepts—velocity distribution, frictional effects, and flow regime transitions—within realistic biomedical-type geometries. Rather than focusing on precise quantitative calibration, the simulations aimed to reveal qualitative flow trends such as acceleration, shear, and secondary motion.

1) Objectives and Selected Geometries: Three geometries were designed to represent characteristic internal flow cases often encountered in biomedical systems:

- **Elbow pipe:** a 90° curved conduit analogous to catheter bends or vascular turns.
- **Aorta-like bifurcation:** a curved, branching model inspired by the human aortic arch, used to study division of flow and curvature-induced stress.
- **Multi-inlet circular junction:** a configuration with two merging inlets and one outlet, analogous to venous or perfusion junctions.

All geometries were created and meshed with triangular finite elements to ensure adequate resolution of curved boundaries and junctions.

2) Governing Equations: The simulations solved the steady, incompressible **Navier–Stokes equations** for laminar flow:

$$\nabla \cdot \vec{v} = 0, \quad \rho(\vec{v} \cdot \nabla)\vec{v} = -\nabla p + \mu\nabla^2\vec{v},$$

where ρ is the fluid density, μ the dynamic viscosity, \vec{v} the velocity vector, and p the static pressure. These equations describe momentum conservation and viscous diffusion within a Newtonian fluid—sufficient for modeling low-to-moderate Reynolds-number biomedical flows.

3) Boundary Conditions: Boundary conditions were defined to replicate generic internal conduit conditions:

- A uniform velocity inlet profile.
- A zero-gauge pressure outlet condition.
- No-slip walls where $\vec{v} = 0$.

This configuration enforces physically realistic flow confinement and allows comparison of internal velocity development among geometries.

4) Meshing and Numerical Solution: Each domain was discretized using an unstructured triangular mesh, refined near walls and curvature zones to capture high velocity gradients. The laminar solver in FEAtool employed the finite-element method (FEM) with a segregated pressure–velocity coupling algorithm. Convergence criteria were set such that residuals fell below 10^{-6} , ensuring numerical stability and smooth velocity fields across the entire domain. To ensure reliability, the simulations were also carried using the OpenFoam solver. Visualizations from both solvers matched.

5) Simulation Constraints: All simulations assumed steady-state, incompressible flow of a Newtonian fluid with constant properties. All models were simulated under steady, incompressible flow conditions. Blood was chosen as the working fluid, with density $\rho = 1300 \text{ kg/m}^3$ and viscosity $\mu = 3 \times 10^{-3} \text{ Pa.s}$.

6) Purpose Within the Task: This CFD component serves as the *bonus extension* of the project methodology. It complements the analytical MATLAB app by providing field-level visualization of how Reynolds number concepts manifest spatially. The subsequent section (*Results & Discussion*) presents the full visual outcomes—velocity contours, arrows, and streamlines—for each geometry, interpreting their physical and biomedical significance.

III. RESULTS AND DISCUSSION

A. Part 1: Reynolds Number Calculator and Flow Regime Classification

The tabulated results from the calculations at various conditions in shown in figure 1. It's obvious that the value of Reynold's number changes as the geometry itself changes either in the hydraulic diameter or the geometric cross section itself. It is noteworthy, however, that the value of Reynold's number for the same geometry and diameter changes as the temperature rises. This makes scientific sense because a higher temperature means higher kinetic energy for the fluid molecules, which increases the change of turbulence in the same geometry. It is also worth noting that transitional flows do not have a defined value of the friction factor. This is because, while equations exist for the friction factor at turbulent and laminar flows, there isn't a concrete equation for transitional flows. Therefore, it is often calculated using interpolations. We decided to rely only on concrete formulas instead of interpolations and, therefore, labeled friction factor in translational flows as NAN.

HydraulicDiameter	Configuration	Diameter	Velocity m/s	HydraulicDiameter / D	ReynoldsNumber	FlowRegime	FrictionFactor
Water 100	Rectangular (W0.25,D=0.1)	W0.25, D=0.1	0.1000	0.1000	1.4220e+03	Laminar	0.0460
Water 100	Rectangular (W0.25,D=0.1)	W0.25, D=0.1	0.5000	0.5000	7.1556e+03	Turbulent	0.0344
Water 100	Rectangular (W0.25,D=0.1)	W0.25, D=0.1	1.0000	0.5000	1.4220e+03	Turbulent	0.0344
Water 100	Rectangular (W0.25,D=0.1)	W0.25, D=0.1	2.0000	0.5000	2.8440e+03	Turbulent	0.0344
Water 100	Annulus (D=0.1, D=0.05)	D=0.1, D=0.05	0.1000	0.0500	4.9016e+02	Turbulent	0.0377
Water 100	Annulus (D=0.1, D=0.05)	D=0.1, D=0.05	0.5000	0.0500	2.4505e+03	Turbulent	0.0352
Water 100	Annulus (D=0.1, D=0.05)	D=0.1, D=0.05	1.0000	0.0500	4.9016e+02	Turbulent	0.0377
Water 100	Annulus (D=0.1, D=0.05)	D=0.1, D=0.05	2.0000	0.0500	9.8032e+02	Turbulent	0.0378
Water 100	Annulus (D=0.05, D=0.025)	D=0.05, D=0.025	0.1000	0.0500	2.3958e+04	Transitional	NAN
Water 100	Annulus (D=0.05, D=0.025)	D=0.05, D=0.025	0.5000	0.0500	1.4220e+03	Laminar	0.0460
Water 100	Annulus (D=0.05, D=0.025)	D=0.05, D=0.025	1.0000	0.0500	2.3958e+04	Transitional	NAN
Water 100	Annulus (D=0.05, D=0.025)	D=0.05, D=0.025	2.0000	0.0500	5.9772e+04	Turbulent	0.0302
Water 100	Annulus (D=0.05, D=0.025)	D=0.05, D=0.025	0.1000	0.0100	1.4220e+03	Laminar	0.0460
Water 100	Annulus (D=0.05, D=0.025)	D=0.05, D=0.025	0.5000	0.0100	7.1556e+03	Turbulent	0.0344
Water 100	Annulus (D=0.05, D=0.025)	D=0.05, D=0.025	1.0000	0.0100	1.4220e+03	Laminar	0.0460
Water 100	Annulus (D=0.05, D=0.025)	D=0.05, D=0.025	2.0000	0.0100	2.8440e+03	Turbulent	0.0344
Water 100	Annulus (D=0.05, D=0.025)	D=0.05, D=0.025	0.1000	0.0050	3.9397e+04	Turbulent	NAN
Water 100	Annulus (D=0.05, D=0.025)	D=0.05, D=0.025	0.5000	0.0050	1.7950e+04	Turbulent	0.0377
Water 100	Annulus (D=0.05, D=0.025)	D=0.05, D=0.025	1.0000	0.0050	3.9397e+04	Turbulent	0.0377
Water 100	Annulus (D=0.05, D=0.025)	D=0.05, D=0.025	2.0000	0.0050	7.1974e+04	Turbulent	0.0393
Water 100	Annulus (D=0.05, D=0.025)	D=0.05, D=0.025	0.1000	0.0025	7.1974e+04	Turbulent	0.0393
Water 100	Annulus (D=0.05, D=0.025)	D=0.05, D=0.025	0.5000	0.0025	1.4220e+03	Laminar	0.0460
Water 100	Annulus (D=0.05, D=0.025)	D=0.05, D=0.025	1.0000	0.0025	3.9397e+04	Turbulent	0.0377
Water 100	Annulus (D=0.05, D=0.025)	D=0.05, D=0.025	2.0000	0.0025	7.1974e+04	Turbulent	0.0393
Water 100	Annulus (D=0.05, D=0.025)	D=0.05, D=0.025	0.1000	0.0010	1.4220e+03	Laminar	0.0460
Water 100	Annulus (D=0.05, D=0.025)	D=0.05, D=0.025	0.5000	0.0010	1.4220e+03	Laminar	0.0460
Water 100	Annulus (D=0.05, D=0.025)	D=0.05, D=0.025	1.0000	0.0010	1.4220e+03	Laminar	0.0460
Water 100	Annulus (D=0.05, D=0.025)	D=0.05, D=0.025	2.0000	0.0010	1.4220e+03	Laminar	0.0460
Water 100	Annulus (D=0.05, D=0.025)	D=0.05, D=0.025	0.1000	0.0005	1.4220e+03	Laminar	0.0460
Water 100	Annulus (D=0.05, D=0.025)	D=0.05, D=0.025	0.5000	0.0005	1.4220e+03	Laminar	0.0460
Water 100	Annulus (D=0.05, D=0.025)	D=0.05, D=0.025	1.0000	0.0005	1.4220e+03	Laminar	0.0460
Water 100	Annulus (D=0.05, D=0.025)	D=0.05, D=0.025	2.0000	0.0005	1.4220e+03	Laminar	0.0460
Water 100	Annulus (D=0.05, D=0.025)	D=0.05, D=0.025	0.1000	0.0001	1.4220e+03	Laminar	0.0460
Water 100	Annulus (D=0.05, D=0.025)	D=0.05, D=0.025	0.5000	0.0001	1.4220e+03	Laminar	0.0460
Water 100	Annulus (D=0.05, D=0.025)	D=0.05, D=0.025	1.0000	0.0001	1.4220e+03	Laminar	0.0460
Water 100	Annulus (D=0.05, D=0.025)	D=0.05, D=0.025	2.0000	0.0001	1.4220e+03	Laminar	0.0460
Water 100	Annulus (D=0.05, D=0.025)	D=0.05, D=0.025	0.1000	0.00005	1.4220e+03	Laminar	0.0460
Water 100	Annulus (D=0.05, D=0.025)	D=0.05, D=0.025	0.5000	0.00005	1.4220e+03	Laminar	0.0460
Water 100	Annulus (D=0.05, D=0.025)	D=0.05, D=0.025	1.0000	0.00005	1.4220e+03	Laminar	0.0460
Water 100	Annulus (D=0.05, D=0.025)	D=0.05, D=0.025	2.0000	0.00005	1.4220e+03	Laminar	0.0460
Water 100	Annulus (D=0.05, D=0.025)	D=0.05, D=0.025	0.1000	0.00001	1.4220e+03	Laminar	0.0460
Water 100	Annulus (D=0.05, D=0.025)	D=0.05, D=0.025	0.5000	0.00001	1.4220e+03	Laminar	0.0460
Water 100	Annulus (D=0.05, D=0.025)	D=0.05, D=0.025	1.0000	0.00001	1.4220e+03	Laminar	0.0460
Water 100	Annulus (D=0.05, D=0.025)	D=0.05, D=0.025	2.0000	0.00001	1.4220e+03	Laminar	0.0460
Water 100	Annulus (D=0.05, D=0.025)	D=0.05, D=0.025	0.1000	0.000005	1.4220e+03	Laminar	0.0460
Water 100	Annulus (D=0.05, D=0.025)	D=0.05, D=0.025	0.5000	0.000005	1.4220e+03	Laminar	0.0460
Water 100	Annulus (D=0.05, D=0.025)	D=0.05, D=0.025	1.0000	0.000005	1.4220e+03	Laminar	0.0460
Water 100	Annulus (D=0.05, D=0.025)	D=0.05, D=0.025	2.0000	0.000005	1.4220e+03	Laminar	0.0460
Water 100	Annulus (D=0.05, D=0.025)	D=0.05, D=0.025	0.1000	0.000001	1.4220e+03	Laminar	0.0460
Water 100	Annulus (D=0.05, D=0.025)	D=0.05, D=0.025	0.5000	0.000001	1.4220e+03	Laminar	0.0460
Water 100	Annulus (D=0.05, D=0.025)	D=0.05, D=0.025	1.0000	0.000001	1.4220e+03	Laminar	0.0460
Water 100	Annulus (D=0.05, D=0.025)	D=0.05, D=0.025	2.0000	0.000001	1.4220e+03	Laminar	0.0460
Water 100	Annulus (D=0.05, D=0.025)	D=0.05, D=0.025	0.1000	0.0000005	1.4220e+03	Laminar	0.0460
Water 100	Annulus (D=0.05, D=0.025)	D=0.05, D=0.025	0.5000	0.0000005	1.4220e+03	Laminar	0.0460
Water 100	Annulus (D=0.05, D=0.025)	D=0.05, D=0.025	1.0000	0.0000005	1.4220e+03	Laminar	0.0460
Water 100	Annulus (D=0.05, D=0.025)	D=0.05, D=0.025	2.0000	0.0000005	1.4220e+03	Laminar	0.0460
Water 100	Annulus (D=0.05, D=0.025)	D=0.05, D=0.025	0.1000	0.0000001	1.4220e+03	Laminar	0.0460
Water 100	Annulus (D=0.05, D=0.025)	D=0.05, D=0.025	0.5000	0.0000001	1.4220e+03	Laminar	0.0460
Water 100	Annulus (D=0.05, D=0.025)	D=0.05, D=0.025	1.0000	0.0000001	1.4220e+03	Laminar	0.0460
Water 100	Annulus (D=0.05, D=0.025)	D=0.05, D=0.025	2.0000	0.0000001	1.4220e+03	Laminar	0.0460
Water 100	Annulus (D=0.05, D=0.025)	D=0.05, D=0.025	0.1000	0.00000005	1.4220e+03	Laminar	0.0460
Water 100	Annulus (D=0.05, D=0.025)	D=0.05, D=0.025	0.5000	0.00000005	1.4220e+03	Laminar	0.0460
Water 100	Annulus (D=0.05, D=0.025)	D=0.05, D=0.025	1.0000	0.00000005	1.4220e+03	Laminar	0.0460
Water 100	Annulus (D=0.05, D=0.025)	D=0.05, D=0.025	2.0000	0.00000005	1.4220e+03	Laminar	0.0460
Water 100	Annulus (D=0.05, D=0.025)	D=0.05, D=0.025	0.1000	0.00000001	1.4220e+03	Laminar	0.0460
Water 100	Annulus (D=0.05, D=0.025)	D=0.05, D=0.025	0.5000	0.00000001	1.4220e+03	Laminar	0.0460
Water 100	Annulus (D=0.05, D=0.025)	D=0.05, D=0.025	1.0000	0.00000001	1.4220e+03	Laminar	0.0460
Water 100	Annulus (D=0.05, D=0.025)	D=0.05, D=0.025	2.0000	0.00000001	1.4220e+03	Laminar	0.0460
Water 100	Annulus (D=0.05, D=0.025)	D=0.05, D=0.025	0.1000	0.000000005	1.4220e+03	Laminar	0.0460
Water 100	Annulus (D=0.05, D=0.025)	D=0.05, D=0.025	0.5000	0.000000005	1.4220e+03	Laminar	0.0460
Water 100	Annulus (D=0.05, D=0.025)	D=0.05, D=0.025	1.0000	0.000000005	1.4220e+03	Laminar	0.0460
Water 100	Annulus (D=0.05, D=0.025)	D=0.05, D=0.025	2.0000	0.000000005	1.4220e+03	Laminar	0.0460
Water 100	Annulus (D=0.05, D=0.025)	D=0.05, D=0.025	0.1000	0.000000001	1.4220e+03	Laminar	0.0460
Water 100	Annulus (D=0.05, D=0.025)	D=0.05, D=0.025	0.5000	0.000000001	1.4220e+03	Laminar	0.0460
Water 100	Annulus (D=0.05, D=0.025)	D=0.05, D=0.025	1.0000	0.000000001	1.4220e+03	Laminar	0.0460
Water 100	Annulus (D=0.05, D=0.025)	D=0.05, D=0.025	2.0000	0.000000001	1.4220e+03	Laminar	0.0460
Water 100	Annulus (D=0.05, D=0.025)	D=0.05, D=0.025	0.1000	0.0000000005	1.4220e+03	Laminar	0.0460
Water 100	Annulus (D=0.05, D=0.025)	D=0.05, D=0.025	0.5000	0.0000000005	1.4220e+03	Laminar	0.0460
Water 100	Annulus (D=0.05, D=0.025)	D=0.05, D=0.025	1.0000	0.0000000005	1.4220e+03	Laminar	0.0460
Water 100	Annulus (D=0.05, D=0.025)	D=0.05, D=0.025	2.0000	0.0000000005	1.4220e+03	Laminar	0.0460
Water 100	Annulus (D=0.05, D=0.025)	D=0.05, D=0.025	0.1000	0.0000000001	1.4220e+03	Laminar	0.0460
Water 100	Annulus (D=0.05, D=0.025)	D=0.05, D=0.025	0.5000	0.0000000001	1.4220e+03	Laminar	0.0460
Water 100	Annulus (D=0.05, D=0.025)	D=0.05, D=0.025	1.0000	0.0000000001	1.4220e+03	Laminar	0.0460
Water 100	Annulus (D=0.05, D=0.025)	D=0.05, D=0.025	2.0000	0.0000000001	1.4220e+03	Laminar	0.0460
Water 100	Annulus (D=0.05, D=0.025)	D=0.05, D=0.025	0.1000	0.00000000005	1.4220e+03	Laminar	0.0460
Water 100	Annulus (D=0.05, D=0.025)	D=0.05, D=0.025	0.5000				

is an estimation of what the turbulent flow would have looked like.

The laminar profile (Fig. 2) exhibits a clear parabolic shape with maximum velocity at the pipe centreline and zero at the wall. The turbulent profile (Fig. 3) is flatter, showing greater uniformity due to momentum exchange by turbulent eddies. The transitional regime was not explicitly visualised because no unique analytical solution exists for it.

From a biomedical standpoint, laminar flow characterises most small-vessel blood motion, ensuring smooth mass transport, whereas turbulent flow is expected at high-velocity zones such as the aortic arch, where chaotic mixing and shear forces occur.

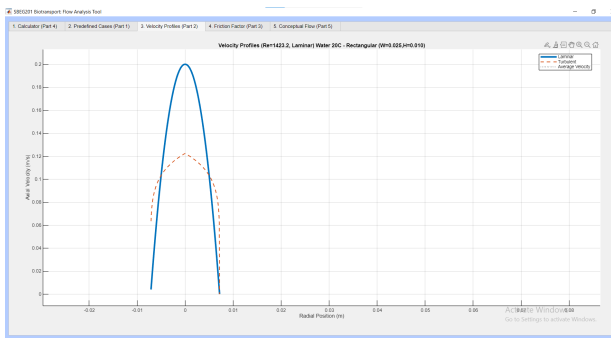


Fig. 2. Laminar velocity profile for $Re = 1423.2$; parabolic distribution with maximum velocity at the pipe centreline.

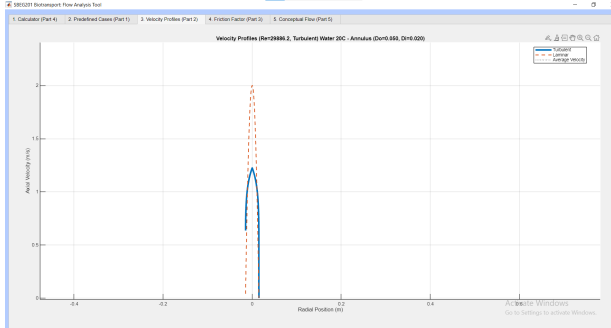


Fig. 3. Turbulent velocity profile for $Re = 4981.0$; flatter distribution due to enhanced momentum transfer by eddies.

The MATLAB app also enabled interactive computation of these profiles (Fig. 4), where the user inputs parameters to instantly generate both curves for comparison.

It is also worth noting that turbulent flows are always smaller in magnitude than laminar flows. This is mainly because of how kinetic energy (from inlet velocity or applied pressure) is distributed in both flows. The laminar flow moves uniformly in a single direction with the application of kinetic energy. Therefore, the energy is efficiently consumed in moving the flow only. On the other hand, turbulent flows are characterized by their chaotic nature. The application of kinetic energy results in the fluid moving in loops, curves, and otherwise inefficient motion that opposes the flow itself. Therefore, they are always smaller in velocity magnitude than laminar flows. —

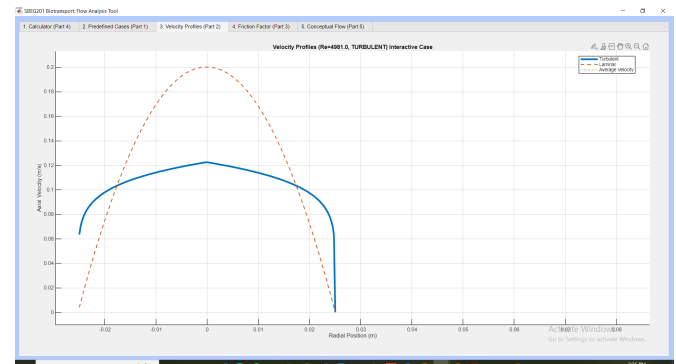


Fig. 4. Velocity profile obtained interactively from the MATLAB calculator, plotting the actual turbulent model and the predicted laminar model using the 1/7th power law

C. Part 3: Reynolds Number Effects on Friction Factor

The relationship between Reynolds number and Darcy friction factor was plotted on a logarithmic scale, replicating the classical Moody chart behaviour (Fig. 5). This behaviour matched empirical charts from Cengel and the Nuclear Power Darcy friction factor reference, confirming the accuracy of the backend computation. The rougher materials (e.g., rusted steel, old pipes) showed higher friction, while smooth surfaces (plastic, tubing) produced lower values at the same Reynolds number.

In biological terms, surface roughness analogues include arterial wall irregularities or plaque deposits that can elevate local friction losses and affect pressure regulation.

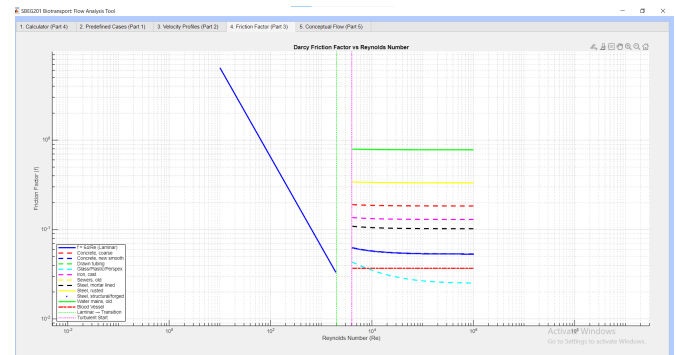


Fig. 5. Log-log plot of Darcy friction factor versus Reynolds number, illustrating laminar, transitional, and turbulent regimes for various surface roughnesses.

D. Part 4: Interactive Calculator

The interactive MATLAB calculator (Fig. 6) was designed to simplify the analysis of flow regimes and friction factors for any user-defined inputs. The app allows entry of density, velocity, viscosity, and geometry type (pipe, duct, annulus, etc.), automatically computing the Reynolds number and flow regime.

A color-coded indicator system was used:

- Green for laminar flow
- Orange for transitional flow
- Red for turbulent flow

The transitional case returns undefined friction factors (NaN) because the mathematical model is indeterminate in this range. This correlation offers a non-iterative, efficient implementation of the Colebrook relation, enhancing educational clarity while maintaining computational accuracy.

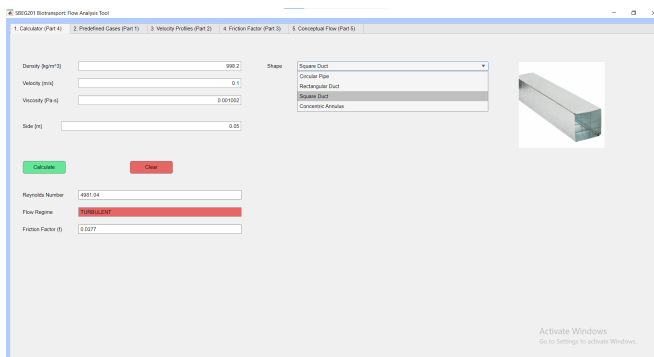


Fig. 6. Interactive MATLAB calculator interface showing input parameters, calculated Reynolds number, flow regime, and friction factor.

E. Part 5: Conceptual Flow Regime Visualization

The final section provided a conceptual representation of laminar, transitional, and turbulent flow using quiver plots (Fig. 7). These diagrams visually convey how fluid motion evolves as Reynolds number increases.

- **Laminar flow:** Streamlines are smooth, parallel, and equally spaced—representing uniform velocity and minimal energy loss.
- **Transitional flow:** Streamlines become wavy and unstable, signifying the onset of oscillations and mixing.
- **Turbulent flow:** The motion becomes chaotic, with random vector directions and fluctuating magnitudes, indicating strong mixing and high energy dissipation.

Physically, this reflects how energy from a uniform inlet velocity disperses within the flow field. In laminar cases, energy remains coherent and aligned, while in turbulence it spreads randomly, reducing the collective average velocity but enhancing momentum and mass transfer.

These results closely match the conceptual visualisations in Cengel's Fluid Mechanics textbook and illustrate fundamental flow behaviour essential in biomedical devices such as catheters, arterial grafts, and microfluidic systems.

BONUS PART: CFD SIMULATION AND FLOW VISUALIZATION IN COMPLEX GEOMETRIES

F. Two-Inlet and One-Outlet Pipe Geometry

In this configuration, the two incoming streams converge into a single outlet, forming a merging flow region. Initially, the velocity vectors at both inlets were uniform, producing a symmetric, laminar entry profile. As the two jets merged, local

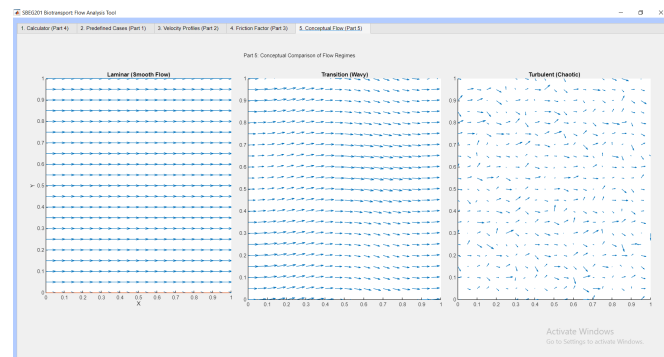


Fig. 7. Conceptual quiver plots showing laminar (smooth), transitional (wavy), and turbulent (chaotic) velocity fields.

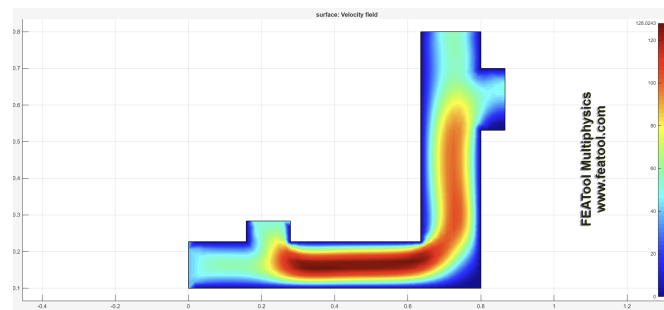


Fig. 8. Base geometry and boundary conditions for the two-inlet, one-outlet configuration.

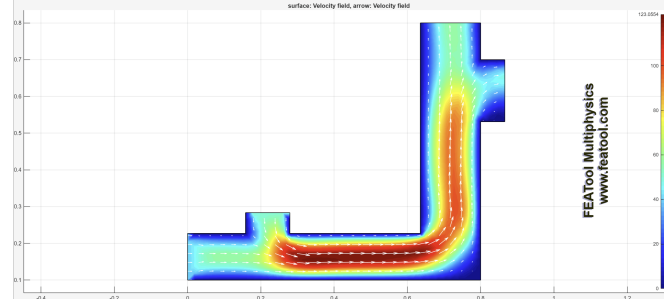


Fig. 9. Velocity vectors showing uniform entry at both inlets and merging flow downstream.

acceleration occurred near the junction centreline, raising local Reynolds number and triggering small recirculation zones near the walls.

The contours confirm that the centre region experiences higher velocity due to flow superposition, while the walls show low-speed boundary layers. This transition from parallel laminar streams to a disturbed merging profile demonstrates how turbulence can arise in converging biomedical junctions such as arterial bifurcations.

G. Multi-Inlet Circular Pipe

This simulation demonstrates how multiple inlets feeding into a single circular outlet enhance turbulent behaviour. The impinging jets from the inlets produced high-velocity zones and overlapping shear layers that destabilised the flow.

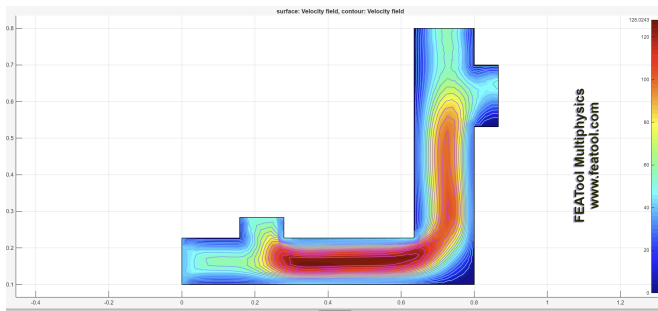


Fig. 10. Velocity contour distribution illustrating gradual acceleration at the merging region.

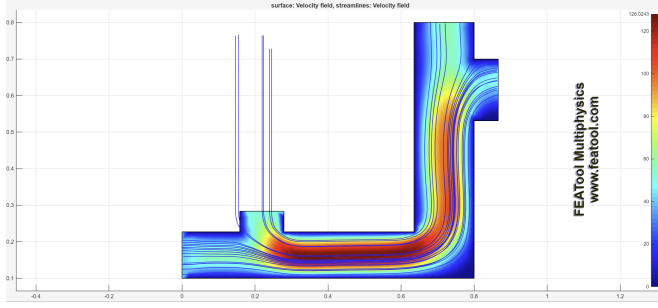


Fig. 11. Streamlines indicating smooth merging and limited turbulence at moderate Reynolds number.

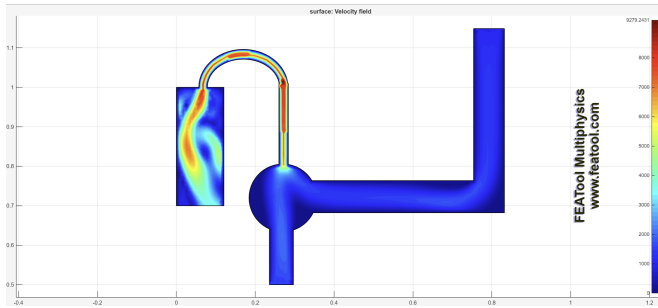


Fig. 12. Multi-inlet circular pipe geometry. Each inlet introduces a separate jet into the main chamber.

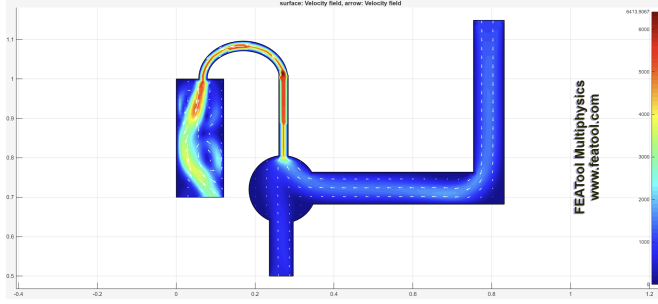


Fig. 13. Velocity vectors showing rapid mixing of streams from multiple inlets.

The contours and streamlines reveal rapid mixing and the emergence of small-scale vortices, typical of fully turbulent internal flow.

This configuration is particularly relevant to biomedical flow systems such as oxygenators or dialysis devices, where

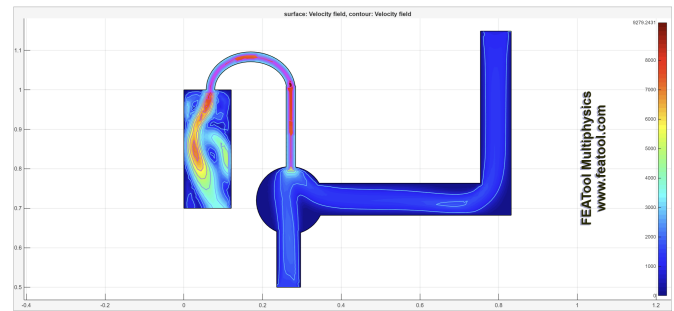


Fig. 14. Velocity contours revealing strong shear layers and recirculation near the wall.

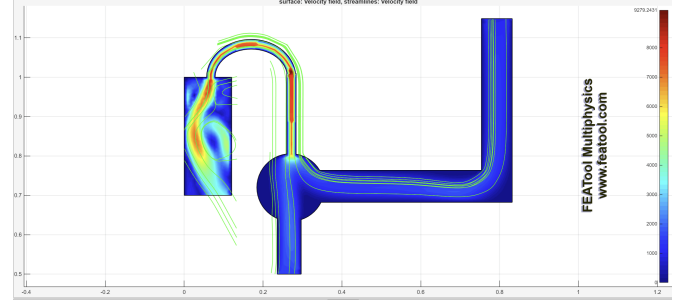


Fig. 15. Streamlines confirming mixing-induced turbulence and vortex formation.

multiple inflows must mix efficiently before exiting through a single port. The high shear rates observed here can promote mixing but may also elevate the risk of hemolysis in blood-handling devices.

H. Aorta

The aorta CFD simulation represents a realistic case of pulsatile, blood flow through a complex, branching geometry. As the flow exits the heart and enters the ascending aorta, it experiences rapid acceleration and curvature-induced effects due to the vessel's natural arch. It's proven in science that the aorta is the main turbulent artery in the human body due to its arched and curved nature [5], which is shown in the simulation.

I. Overall Discussion and Physical Insights

Across all simulated models, the following physical phenomena were observed:

- Flow starts laminar and becomes progressively disturbed when subjected to geometric asymmetry, high velocity, or merging streams.
- Velocity contours show consistent acceleration at constricted or curved regions and deceleration at expansion or merging zones.
- Streamline plots confirm that turbulence first appears near boundaries, then propagates into the core.
- The transition to turbulence corresponds with local Reynolds number increase, consistent with analytical results.

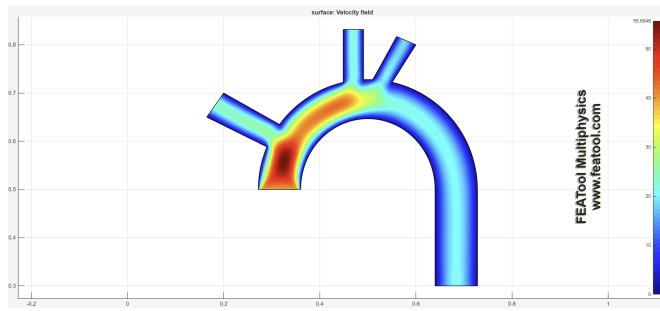


Fig. 16. Aorta geometry showing the inlet from the heart and the 4 outflow arteries

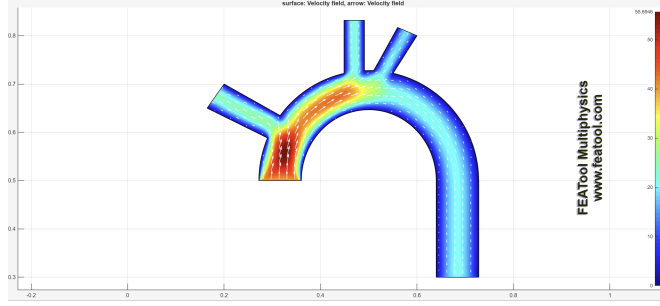


Fig. 17. Velocity vectors showing laminar inflow and curved acceleration through the bends

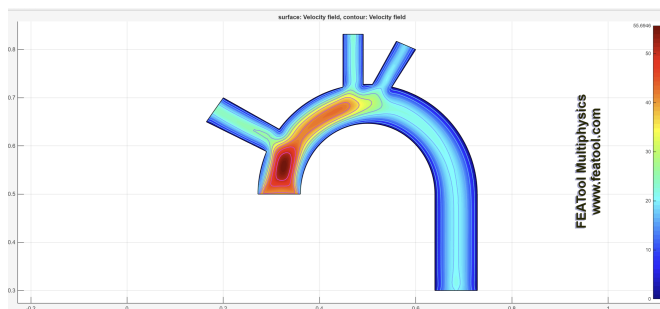


Fig. 18. Velocity contour plot showing acceleration along the bend and deceleration near the walls.

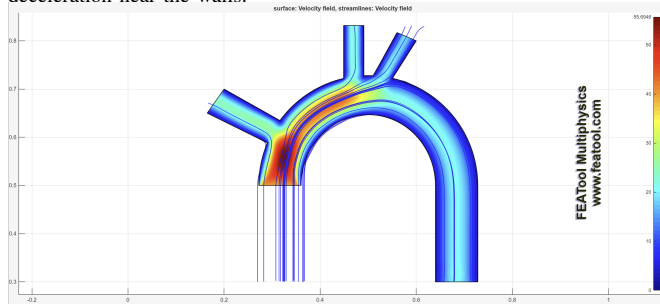


Fig. 19. Streamlines highlighting turbulence through the bend

The combined analytical and computational analysis provides a comprehensive understanding of internal flow transitions. The MATLAB-based analytical tool predicts the onset of turbulence quantitatively, while CFD visualisations reveal the detailed structure and energy distribution of the flow field.

These findings bridge theoretical understanding and phys-

ical intuition, directly applicable to biomedical systems such as blood flow through curved arteries, mixing in perfusion devices, and flow optimisation in prosthetic vascular grafts.

IV. CONCLUSION

Through the combination of analytical modeling and computational visualization, this study demonstrated how the Reynolds number fundamentally dictates flow behavior in internal conduits. The MATLAB-based tool provided a clear quantitative understanding of how variations in fluid properties, geometry, and velocity influence the flow regime, while the CFD simulations translated these effects into physical flow patterns.

For low Reynolds numbers ($Re < 2000$), the flow remained laminar, characterized by smooth, parallel streamlines and a parabolic velocity distribution with maximum speed at the centreline. As Re increased to the transitional range ($2000 \leq Re < 4000$), flow disturbances began to appear, though without a fixed analytical expression, reflecting the unstable and mixed nature of this regime. For turbulent flow ($Re \geq 4000$), the velocity profile became increasingly flat due to momentum diffusion by eddies, and the friction factor decreased according to the Swamee–Jain correlation, consistent with theoretical expectations and Moody chart trends.

The CFD results reinforced these analytical findings by visually capturing the progressive transition from laminar to turbulent motion across different geometries. Velocity contours and streamlines confirmed that higher Reynolds numbers and curved or merging geometries induce secondary flows, vortices, and regions of energy loss. Such effects are directly relevant in biomedical contexts—such as blood flow through arteries, catheters, and prosthetic channels—where flow regime shifts can alter wall shear stress and affect device safety or physiological response.

Overall, the study highlighted that the Reynolds number not only determines the onset of turbulence but also governs energy dissipation, velocity distribution, and flow uniformity. Understanding this relationship is essential for designing efficient and biocompatible systems in biomedical engineering, where controlling flow behavior directly impacts patient safety and device performance.

REFERENCES

- [1] Y. A. Cengel and J. M. Cimbala, *Fluid Mechanics: Fundamentals and Applications*, 3rd ed. New York, NY: McGraw-Hill Education, 2018.
- [2] FEATool Multiphysics, “CFD and Multiphysics Simulation Platform.” [Online]. Available: <https://www.featool.com/>. [Accessed: Oct. 23, 2025].
- [3] EngineerExcel, “Swamee–Jain Equation for Friction Factor,” [Online]. Available: <https://engineerexcel.com/swamee-jain-equation/>. [Accessed: Oct. 23, 2025].
- [4] Nuclear Power, “Darcy Friction Factor for Laminar Flow,” [Online]. Available: <https://nuclear-power.com/wp-content/uploads/2016/06/darcy-friction-factor-for-laminar-flow.png>. [Accessed: Oct. 23, 2025].
- [5] Stein, P. D., & Sabbah, H. N. (1976). Turbulent blood flow in the ascending aorta of humans with normal and diseased aortic valves. *Circulation Research*, 39(1), 58–65. <https://doi.org/10.1161/01.res.39.1.58>